Naval Research Laboratory

Stennis Space Center, MS 39529-5004

NRL/MR/7322--19-9903

Floe Size Mapping from Satellite SAR Images and Icewatch Observations in the Beaufort Sea during Autumn 2015

Gleb G. Panteleev
W. Erick Rogers
Max Yaremchuk
Tamara Townsend

Ocean Dynamics and Prediction Branch
Oceanography Division

Hui Shen

Bedford Institute of Oceanography
Nova Scotia, Canada

Luc Rainville

Applied Physics Laboratory, University of Washington
Seattle, WA

Julia Crout

Perpsecta
Stennis Space Center, MS

July 26, 2019

REPORT DOCUMENTATION PAGE

Form Approved
OMB No. 0704-0188

1. REPORT DATE *(DD-MM-YYYY)*	**2. REPORT TYPE**	**3. DATES COVERED** *(From - To)*
26-07-2019	NRL Memorandum Report	

4. TITLE AND SUBTITLE

Floe Size Mapping from Satellite SAR Images and Icewatch Observations in the Beaufort Sea during Autumn 2015

5a. CONTRACT NUMBER

5b. GRANT NUMBER

5c. PROGRAM ELEMENT NUMBER
62435N

6. AUTHOR(S)

Gleb G. Panteleev, W. Erick Rogers, Max Yaremchuk, Tamara L. Townsend, Hui Shen*, Luc Rainville**, and Julia Crout***

5d. PROJECT NUMBER
73-6A50-09-5

5e. TASK NUMBER
BE-435-040

5f. WORK UNIT NUMBER
6A50

7. PERFORMING ORGANIZATION NAME(S) AND ADDRESS(ES)

Naval Research Laboratory
4555 Overlook Avenue, SW
Washington, DC 20375-5320

8. PERFORMING ORGANIZATION REPORT NUMBER

NRL/MR/7322--19-9903

9. SPONSORING / MONITORING AGENCY NAME(S) AND ADDRESS(ES)

Office of Naval Research
One Liberty Center
875 North Randolph Street, Suite 1425
Arlington, VA 22203-1995

10. SPONSOR / MONITOR'S ACRONYM(S)

ONR

11. SPONSOR / MONITOR'S REPORT NUMBER(S)

12. DISTRIBUTION / AVAILABILITY STATEMENT

DISTRIBUTION STATEMENT A: Approved for public release distribution is unlimited.

13. SUPPLEMENTARY NOTES

*Bedford Institute of Oceanography, Challenger Drive, P.O. Box 1006, Dartmouth, Nova Scotia, Canada B2Y 4A2; **Applied Physics Laboratory, University of Washington, 1013 NE 40th Street, Seattle, WA 98105-6606, ***Perspecta, 1103 Balch Blvd, John C. Stennis Space Center, MS 39529-0001

14. ABSTRACT

An approach for automatic detection of the sea ice type in the MIZ from RADARSAT-2 SAR images with HH polarization and resolution of 50 m has been developed and tested. The approach is based on texture analysis using the GLCM (Gray-Level Co-occurrence Matrix) method and several additional functions based on the estimates of the averaged gradient tensor. A machine learning technique ("Support Vector Machine," or SVM) is applied to imagery of ice taken for the region of the Beaufort Sea in autumn 2015, with observations of ice type from two ship cruises used as ground truth. It is found that this method shows promise, but the training requires more collocations than is practical at present-specifically, the ubiquitous inhomogeneity of ice presents a challenge for colocation, as it limits the training set.

15. SUBJECT TERMS

Marginal ice zone, Synthetic aperture radar, Machine learning
Texture analysis Sea ice Wave-ice interactions

16. SECURITY CLASSIFICATION OF:			**17. LIMITATION OF ABSTRACT**	**18. NUMBER OF PAGES**	**19a. NAME OF RESPONSIBLE PERSON**
					W. Erick Rogers
a. REPORT	**b. ABSTRACT**	**c. THIS PAGE**	Unclassified Unlimited	25	**19b. TELEPHONE NUMBER** *(include area code)*
Unclassified Unlimited	Unclassified Unlimited	Unclassified Unlimited			(228) 688-4727

This page intentionally left blank.

Table of Contents

This page intentionally left blank.

Executive Summary

An approach for automatic detection of the sea ice type in the MIZ from RADARSAT-2 SAR images with HH polarization and resolution of 50 m has been developed and tested. The approach is based on texture analysis using the GLCM (Gray-Level Co-occurrence Matrix) method and several additional functions based on the estimates of the averaged gradient tensor. A machine learning technique ("Support Vector Machine" or SVM) is applied to imagery of ice taken for the region of the Beaufort Sea in autumn 2015, with observations of ice type from two ship cruises used as ground truth. It is found that the method shows promise but the training requires more collocations than is practical at present. Specifically, the ubiquitous inhomogeneity of ice presents a challenge for colocation, as it limits the training set.

This page intentionally left blank.

1. Introduction.

The type/size of the ice floes and ice thickness are the two most important sea ice characteristics which control the attenuation of the ocean waves in the marginal ice zone (MIZ). Conventionally, the attenuation process includes both dissipation and scattering. Recent observations in the ice pack, far from MIZ indicate that scattering plays a negligible role in the attenuation of long swells (Ardhuin et al., 2016). Early observation in the Antarctic MIZ shows that amplitude of the short waves significantly decays when sea waves penetrate into MIZ and almost negligible near the interior boundary of the MIZ (Doble and Wadhams, 2006). More recent, observations indicate that sea waves (SW) attenuation also significantly depend on wave frequency, ice thickness and horizontal sizes of the sea ice floes (Doble, 2009, Doble et al., 2015).

Accurate mapping of the areas with different ice types and thickness is important for accurate modeling of the propagation of ocean waves in the MIZ, ocean wave forecasting, and validation of different attenuation models developed during the last decades [Wang and Shen, 2010, Squire and Montiel, 2016, Williams et al., 2013a,b, 2017, Cheng et al. 2017, Thomson et al. 2018, Rogers et al. 2018, Squire, V.A., 2018.

Since 1990's, Synthetic Aperture Radar (SAR) images from various satellites became an important source of the information of the sea surface state. During the last two decades, SAR images were used for determination of sea ice edge, and identification of multiyear, young and new ice, leads, ice velocity and some other ice related parameters ([Zakhvatkina et al, 2013, 2016, Komarov and Barber, 2014)].

Formally, SAR images map the magnitude and phase of the signal backscattered from the ice surface: normalized backscatter coefficient σ_o is the ratio of the radiance of the radar energy reflection back to the radar with corresponding incident angle. SAR images have a typical spatial resolution of between 20 and 50 m and cover relatively wide swath ~400x600 km, although images with higher resolution (~5 m) and smaller footprint (50x50 km) are also available (e.g. COSMO-SkyMed, RISAT-1) Therefore, the most straightforward method for SAR analysis is the development of the microwave scattering model for sea ice surface and obtaining the corresponding inverse solution. However, this approach has several technical problems. The most important is that different sea ice type surfaces have similar values of the backscattering coefficients (Dierking, 2010) and there are many different sea ice characteristics which affect the backwatering signal. There are also essential problem with proper filtering of the contaminating noise and necessity to apply incident angle normalization algorithms, which are also different for different ice types (e.g. Askne et al, 1994, Zakhvatkina et al, 2013)

Because of that, the more advanced method of the ice type identification utilize SAR image texture analysis, which is usually based on the analysis of the Gray Level Co-occurrence Matrix (GLCM) Analysis (e.g. Soh et al., 1999, Clausi, 2002) combined with different kinds of supervised classification algorithms (Support Vector Machine (SVM), Neural Network (NN), and Random Forest (RF)). The efficiency of this approach for identification of the different ice types was successfully demonstrated several publications (e.g. Zakhvatkina et al, 2013, 2016, Bogdanov et al., 2005, Murashkin, et al., 2018).

The typical problem when developing supervised classification algorithms arises from the rarity of *in situ* observation in the dense ice, which are typically conducted from heavy icebreakers. Because of that, many

Manuscript approved July 11, 2019.

authors (e.g. Zakhvatkina et al, 2013) use results of the expert analysis for the supervised training. Formally, that allows one to derive the supervised algorithm with multiple degree of freedom, but from another point of view, expert analysis brings subjectivity into the utilized approach.

In the current report, we analyze applicability of the GLCM analysis and SVM algorithm for identification ice types in the MIZ in the Beaufort Sea using the ship observations from Icewatch Data Network (http://icewatch.gina.alaska.edu/) from two cruises. Our approach roughly, but with some exceptions, followed the strategy proposed by Zakhvatkina et al, (2013) previously applied for the central Arctic for identification of multiyear ice (MYI), deformed first-year ice (FYI) (DFYI), and level FYI (LFYI) and open water/nilas.

The following Sections of the report include description of the in situ observations, available SAR images, and utilized algorithms (GLCM analysis and SVM). After that we discuss results of the analysis and strategy for identification of the different ice type. Conclusions and discussion finalize the Report.

2. Sea ice observations during and ice condition in Fall, 2015.

In situ ice observations have been collected in two cruises. The light icebreaker CCGS "Sir Wilfrid Laurier" conducted the survey of the entire Beaufort Gyre between 9/22/2015 and 10/15/2015 (Figure 1). During this survey, sea ice conditions gradually changed from almost open water conditions extending as far north as 77°N in places, to an autumn condition, when ice covered the major part of the Beaufort Sea with ice concentration ranged between 60% and 100% (Figure 2). The ice-capable R/V Sikuliaq (Polar Class 5), worked in the MIZ in the south-western part of the Beaufort Sea between 10/5/2015 and 11/4/2015 (Figure 1). By the end of this period, Beaufort Sea was completely covered by dense ice.

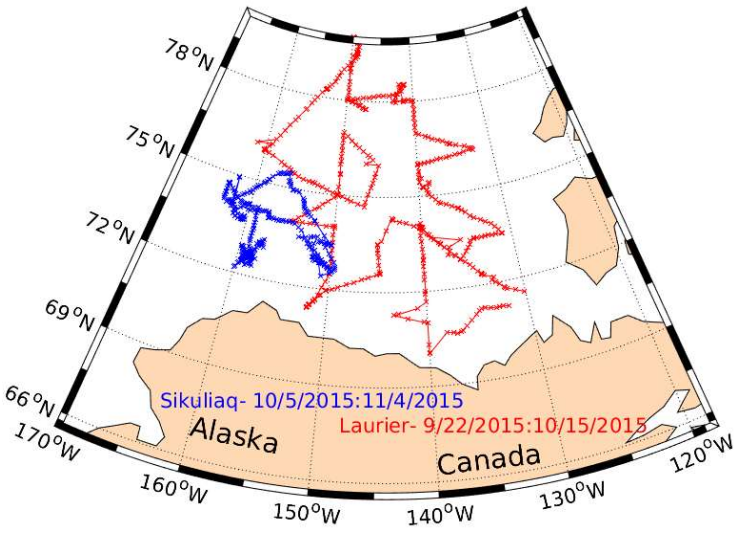

Figure 1. Left: in situ sea ice observation in the Beaufort Sea during Fall, 2015, from R/V Laurier and R/V Sikuliaq and daily averaged ice velocity during October, 15, 2015.

Observation of the sea ice parameters in both cruises were conducted from the ship bridges according to the SIGRID-3 protocol which is associated with the ASSIST web interface (Arctic Shipborne Sea Ice Standardization Tool, http://www.iarc.uaf.edu/icewatch/assist) provided by the 'Ice Watch' program at

the University of Alaska, Fairbanks. Ice observations include: total ice concentration, ice type, ice thickness, floe size, snow type/depth, and description of other features such as sea ice topography, ridge height, topography, melt ponds, etc. The standard set of meteorological parameters include wind speed and direction, air temperature, visibility, and atmospheric pressure. Taking into account that sizes of the floes is an important factor that controls ocean wave attenuation, the primary goal of this study was to map floe sizes observed in the MIZ. Total volume of the sea ice floe size observation was about 400 and 350 from CCGS "Sir Wilfrid Laurier", and R/V Sikuliaq, respectively. A significant part of the sea ice observations were collected in the MIZ, so the observations of the medium (100-500 m), large (500-2000 m) and vast (> 2000 m) floes were rather seldom. Table 1 summarizes the number of the observations of the different ice floe categories. Unfortunately, only about 200 of these observations co-locate with SAR images available to us sampled within a ±1 day temporal window. The critically low (<15) number of the collocation points was found for open water, new sheet ice, brash/broken ice, small/large and vast flow categories.

Numerical data assimilative modeling revealed dynamic sea ice conditions in the Beaufort Sea during the September-December 2015 (Yaremchuk et al., 2018). The experimental sea ice Data Assimilation System (DAS) uses the CICE5 sea ice model (Hunke and Lipscomb, 2008), NCODA approaches (Cummings and Smedstad, 2013) forced by atmospheric fields from the Navy Global Environmental Model (NAVGEM 1.2, Hogan et al., 2014) and oceanic fields from the operational run of the GOFS 3.1 DA system and assimilates sea ice concentration merged from SSMIS and AMSR2 platforms at approximately 5 km resolution.

The maximum sea ice velocities (~0.6-0.8 m/s) were observed during the initial period of the sea ice formation (i.e. October 1-10), but in the MIZ sea ice velocities remained relatively high (~0.2-0.3 m/s) practically for the entire period of our study (e.g. Figure 5 right panel). Detailed analysis of sea ice observations showed that ice floes categories may change significantly between two stations separated by only 5-10 km. Taking into account relatively strong ocean currents, the position of "real" observations can be actually shifted by 10-50 km from the estimated collocation points. That inevitably introduces significant noise into the available sea ice observations and complicates the classification. Because of that, we used SAR images which provided accurate (~6 hours) collocation with sea ice observations and specify an additional set of pseudo-observations in the vicinity of the real sea ice observations overlapping with these SAR images.

In addition, in our analysis we looked at three sea ice concentration product with different resolution. The first product is the daily sea ice passive microwave sea ice concentration fields from National Snow and Ice Data Center (NOAA/NSIDC) with spatial resolution of 25 km https://nsidc.org/data/g02202). The Second is the MASAM2 sea ice concentration (https://nsidc.org/data/g10005). MASAM2 daily 4 km sea ice concentration is a prototype concentration product that is a blend of two other daily sea ice data products: ice coverage from the Multisensor Analyzed Sea Ice Extent (MASIE) product at 4 km resolution and ice concentration from the Advanced Microwave Scanning Radiometer 2 (AMSR2) at 10 km resolution. Third, we also utilized sea ice concentration from the experimental CICE5-NCODA DA described above (Yaremchuk et al., 2018). The daily sea ice concentration maps were spatially and temporally interpolated on the SAR images spatial grid and utilized in the analysis (e.g. Figure 3, 5 right panels).

Table 1. Distribution of the sea ice observation over the ice floes categories. Number in brackets show the additional pseudo-observations generated for the SAR images with relatively accurate collocation with real sea ice observations.

	Pancake	New sheet ice	Brash/ Broken ice	Cake Ice < 20m	Small Floes, 20-100m	Medium Floes, 100-500m	Large floes 500-2000m	Vast floes >2000m	Bergy floes	Open water
S.W.Laurier	20	39	15	93	74	74	49	2	0	48
Sikuliaq	90 (86)	53 (158)	14 (43)	60 (97)	26 (235)	26 (107)	19 (10)	17 (125)	3	60 (313)

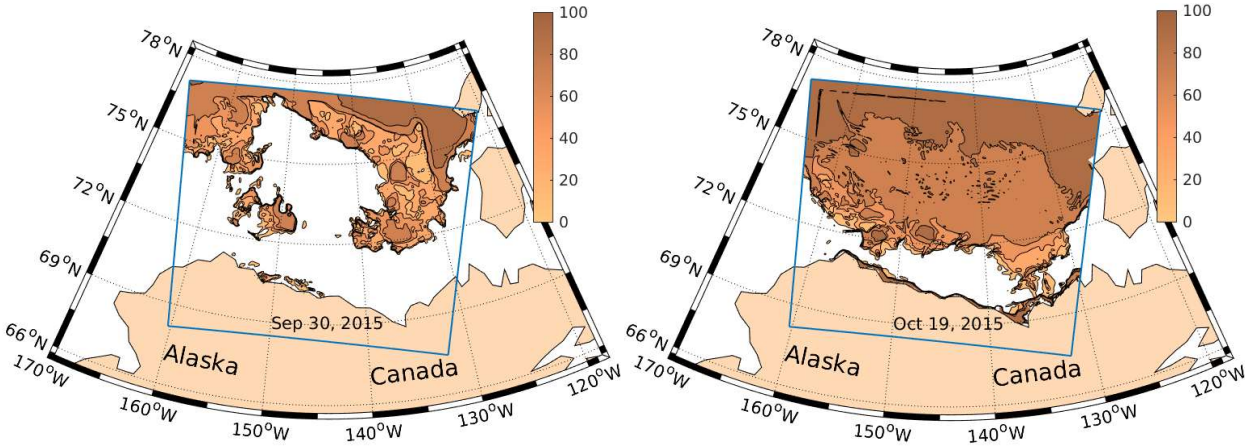

Figure 2. Ice condition (concentration) in the Beaufort Sea during the autumn 2015 from CICE5-NCODA data assimilation system. Dates are indicated within each panel.

3. Acquisition and pre-processing of Satellite Images

In our experiments we used a set (82) of spatially overlapping RADARSAT-2 ScanSAR wide-beam mode image with pixel spacing of 50m, ~450 km swath width) at HH polarization for a period between September 7 and November 7 2015. These are obtained via the National Ice Center (NIC); files are managed and archived by the University of Washington (UW) Applied Physics Laboratory (APL). The images were requested in advance according to the preliminary research plans of both expeditions described above. Unfortunately, the SAR acquisition plans made two or more days in advance did not generally match well the actual ship route. In the case of the R/V Sikuliaq, plans were revised daily (Thomson et al. 2017). Thus, detailed analysis revealed that only 17 images overlap with available in situ observation within temporal window of ±1 day. Only these images were used for the experiments described below. The left panel of Figure 3 shows spatial positions of the utilized SAR images. Table 2 incorporates the list of the SAR images utilized for the analysis and training of the SVM algorithm.

Note that analysis of the results of the numerical experiments with CICE model conducted for the same period of time (Yaremchuk et al., 2018) revealed typical ice velocities about 10 cm/s with maximum speed up to 30-50 cm/s. That results in significant (10-50 km!) inaccuracies in spatial location of the in situ observations taken within ±1 day temporal window with respect to the time of the SAR image. Because of that, relatively high resolution (50 m) SAR images were spatially averaged with 500 m spatial window and resampled. This procedure also decreased speckle noise of the original SAR images. Figure 3 (right panel) shows an example of the spatially averaged SAR with resolution of 500 m. Note, that western part

of the image is blurred due to different backscattering at different incident angles. That is a well-known problem which significantly complicates the image analysis of the SAR images with HH polarization (Lee and Pottier, 2009). In order to address this problem, the available in situ ice floe observations were collocated with SAR images and corresponding σ^o values were plotted against the corresponding incident angle. Unfortunately, the available set of visual sea ice observations allows reliable estimations of angular dependence of the backscattering coefficient only for open water and pancake ice and is less reliable for the cake and medium floes (Figure 4). The volume and/or spatial spreads of other sea ice floes observations were non-sufficient for estimation σ^o dependence of the incident angle.

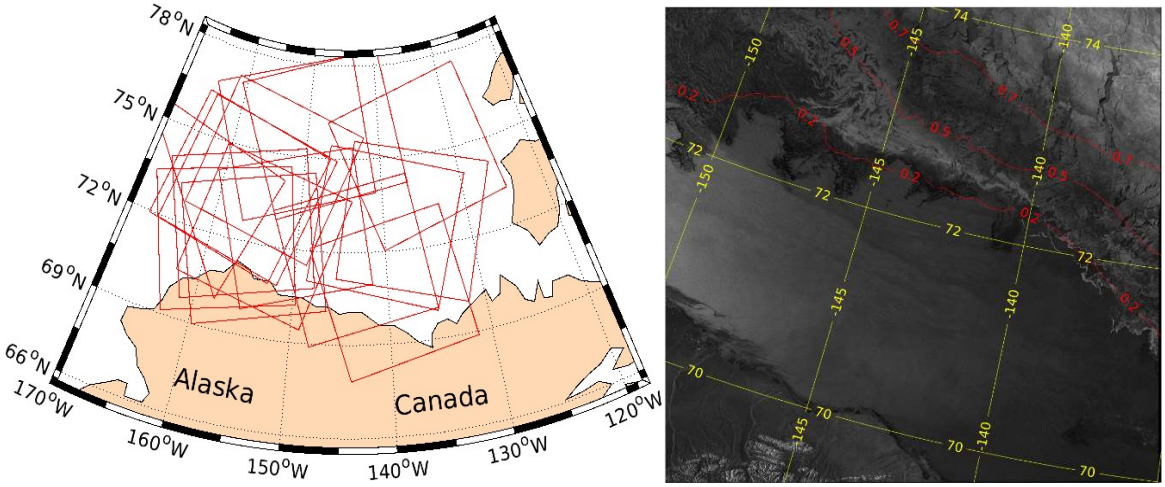

Figure 3. Left panel: Positions of the all images utilized for the training SVM algorithm. Right panel: Radarsat-2 SAR image near the Alaskan coast Oct 10, 2015. All data are provided in GeoTIFF format with auxiliary XML files. Red contours designate the daily sea ice concentration derived from passive microwave sensor according to NSIDC (www.nsdic.org). RADARSAT-2: © MDA 2015.

Typically, σ^o decreases linearly as a function of incident angle. The open water backscattering coefficient has the largest decrease rate (-0.67 dB/^{o}) with respect to the incident angle. The backscattering coefficients for pancake, cake and medium floes decrease with the rates -0.48 dB/^{o}, 0.14 dB/^{o} and -0.58 dB/^{o} respectively. With exception for the cake floes, which probably are not very reliable due to relatively small number of the visual observations, these values are larger than estimated by Kwok and Cunningham, (1994) and Zakhvatkina et al., (2013) for the winter conditions and for the SAR images acquired from different satellites. That is probably due to presence of the open water, which reveal the highest decrease rate, which is comparable with similar estimates conducted by Topouzelis et al. (2016).

The derived quasi-linear angular dependences allows simple re-normalization of σ^o of original SAR images. As an example, Figure 5 shows normalized SAR image derived using the open water σ^o angular dependence (Figure 4). Note, that re-normalization significantly decreased the blurring over the open water regions, while there is still some moderate blurring in the ice covered regions due to different σ^o angular dependence.

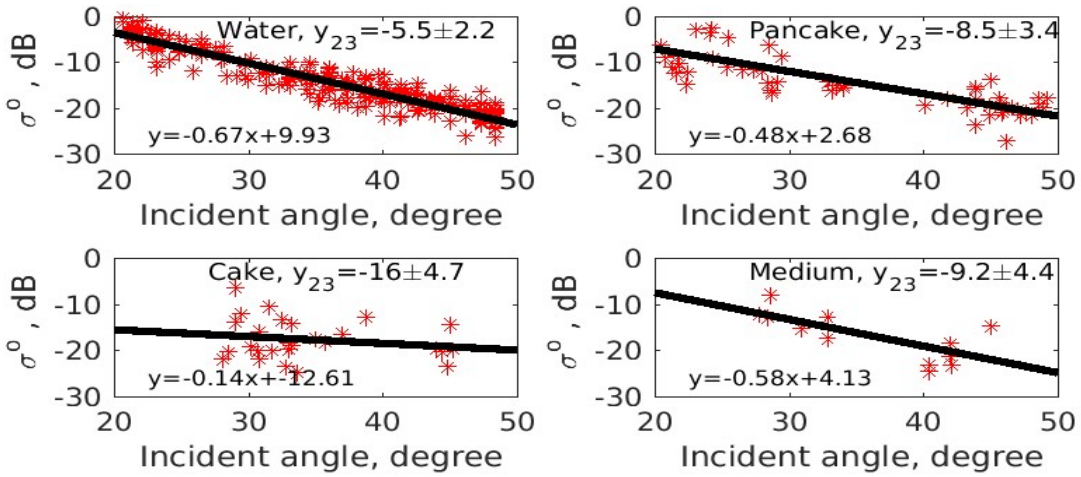

Figure 4. Angular dependence of the backscattering coefficients (б°) for different type of ice. Only real sea ice observations were used.

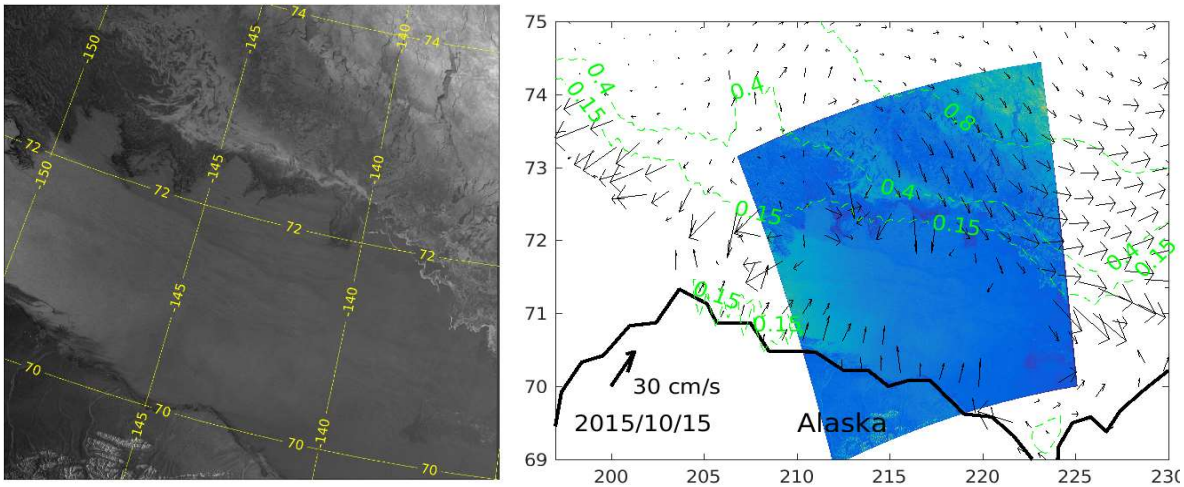

Figure 5. Left: Re-normalized SAR Image with respect open water б° angular dependence. Right –sea ice velocities from CICE-5-NCODA DA model, microwave sea ice concentration (green dashed line) and SAR image during 2015/10/15. RADARSAT-2: © MDA 2015

Table 2. List of the SAR images (Pixel spacing of 50x50m, 520-km swath width), at HH polarization acquired for the Beaufort Sea region between 9 Sep. and 7 Nov. 2015 and used for analysis in this study.

	SAR images for angular dependencies, б° derivations and SVM training/ classification		SAR images for angular dependencies, б° derivations and SVM training/ classification
1	RS2_OK68419_PK633278_DK562983_SCWA_20151022_162006_HH_SGF	32	RS2_OK69418_PK630229_DK559422_SCWA_20151016_022043_HH_SGF
2	RS2_OK68420_PK626204_DK554294_SCWA_20151002_022838_HH_SGF/	33	RS2_OK69418_PK630233_DK559434_SCWA_20151017_152554_HH_SGF
3	RS2_OK68420_PK626206_DK554303_SCWA_20151003_015808_HH_SGF	34	RS2_OK69418_PK630238_DK559443_SCWA_20151019_023205_HH_SGF
4	RS2_OK68420_PK626207_DK554321_SCWA_20151007_014123_HH_SGF	35	RS2_OK69418_PK630239_DK559452_SCWA_20151020_020243_HH_SGF
5	RS2_OK68656_PK625345_DK556405_SCWA_20151024_170237_HH_SGF	36	RS2_OK69418_PK630240_DK559455_SCWA_20151020_020351_HH_SGF
6	RS2_OK68656_PK625762_DK556372_SCWA_20151002_022756_HH_SGF	37	RS2_OK69418_PK630337_DK559437_SCWA_20151018_012210_HH_SGF
7	RS2_OK68656_PK625763_DK556374_SCWA_20151003_171508_HH_SGF	38	RS2_OK69418_PK631965_DK559488_SCWA_20151025_163242_HH_SGF
9	RS2_OK68656_PK625765_DK556376_SCWA_20151006_172741_HH_SGF	39	RS2_OK69418_PK632729_DK559497_SCWA_20151026_160328_HH_SGF
10	RS2_OK68656_PK625766_DK556377_SCWA_20151007_032220_HH_SGF	40	RS2_OK69418_PK633158_DK559473_SCWA_20151023_021630_HH_SGF
11	RS2_OK67811_PK621868_DK551800_SCWA_20150930_170202_HH_SGF	41	RS2_OK69418_PK633303_DK562989_SCWA_20151022_162009_HH_SGF
12	RS2_OK68656_PK625784_DK556385_SCWA_20151015_024847_HH_SGF	42	RS2_OK69482_PK630268_DK559754_SCWA_20151017_033046_HH_SGF
13	RS2_OK68656_PK625810_DK556402_SCWA_20151020_034324_HH_SGF	43	RS2_OK69616_PK635392_DK560718_SCWA_20151106_020633_HH_SGF
14	RS2_OK68656_PK625814_DK556584_SCWA_20151012_023552_HH_SGF	44	RS2_OK69636_PK631259_DK561023_SCWA_20151020_171900_HH_SGF

15	RS2_OK68656_PK629310_DK556379_SCWA_20151009_022346_HH_SGF	45	RS2_OK69636_PK631259_DK561037_SCWA_20151020_171900_HH_SGF
16	RS2_OK68656_PK629312_DK556380_SCWA_20151010_033459_HH_SGF	46	RS2_OK69729_PK632815_DK561483_SCWA_20151102_174013_HH_SGF
17	RS2_OK68656_PK629823_DK556384_SCWA_20151013_034737_HH_SGF	47	RS2_OK69729_PK632816_DK561489_SCWA_20151104_030527_HH_SGF
18	RS2_OK68656_PK630313_DK556397_SCWA_20151016_155548_HH_SGF	48	RS2_OK69729_PK632817_DK561492_SCWA_20151105_023613_HH_SGF
19	RS2_OK68656_PK630324_DK556400_SCWA_20151019_023205_HH_SGF	49	RS2_OK69730_PK632835_DK561588_SCWA_20151102_155916_HH_SGF
20	RS2_OK68656_PK630638_DK556403_SCWA_20151022_024436_HH_SGF	50	RS2_OK69730_PK632840_DK561606_SCWA_20151104_030533_HH_SGF
21	RS2_OK68656_PK631962_DK556407_SCWA_20151026_022755_HH_SGF	51	RS2_OK69730_PK632841_DK561609_SCWA_20151104_030640_HH_SGF
22	RS2_OK68656_PK632790_DK556409_SCWA_20151027_033923_HH_SGF		
23	RS2_OK69226_PK629293_DK558604_SCWA_20151009_022457_HH_SGF		
24	RS2_OK69226_PK629298_DK558629_SCWA_20151015_024958_HH_SGF		
25	RS2_OK69226_PK629301_DK558644_SCWA_20151018_030231_HH_SGF		
26	RS2_OK69226_PK629453_DK558614_SCWA_20151011_030642_HH_SGF		
27	RS2_OK69226_PK629891_DK558624_SCWA_20151014_031919_HH_SGF		
28	RS2_OK69226_PK631608_DK561460_SCWA_20151021_031414_HH_SGF		
29	RS2_OK69226_PK631609_DK561465_SCWA_20151021_031521_HH_SGF		
30	RS2_OK69264_PK629447_DK558857_SCWA_20151010_171023_HH_SGF		
31	RS2_OK69322_PK629903_DK559203_SCWA_20151013_172311_HH_SGF		

4. Texture analysis

4.1 Texture analysis using the Gray-Level Co-Occurrence Matrix (GLCM)

Texture analysis refers to the characterization of regions in an image by their texture content. Texture analysis attempts to quantify intuitive qualities described by terms such as rough, smooth, silky, or bumpy as a function of the spatial variation in pixel intensities. Conventionally, texture analysis is based on the examining the gray-level co-occurrence matrix (GLCM). The GLCM functions characterize the texture of an image by calculating how often pairs of pixel with specific values and in a specified spatial relationship occur in an image, creating a GLCM, and then extracting statistical measures from this matrix.

As given by Haralick et al. (1973) (and other publications such as Soh and Tsatsoulis (1999)), the definition of GLCM is summarized as follows: For any grey image or part of the image I with pixel dimensions $[N_y, N_y]$ we first quantize a scale of the grey levels $G=[0:N_g-1]$ for each pixels of the image. Thus, the image I can be viewed as a function that assigns some gray level to every pair of the coordinates in 2D space $[N_y, N_y]$: $I: [N_y, N_y] \rightarrow G$. The texture information can be determined as a matrix or relative frequencies $P_{r,\gamma}(i,j)$ with two pixels separated by distance d that can be found in the image. Such matrices of gray-level co-occurrence frequencies are a function of the angular relationship γ and distance r between the neighboring pixels. Typically, all angles are quantized by 45°, and additional averaging over the directions can be applied:

$$P_{r,\gamma}(i,j) = \frac{K_{r,\gamma}(i,j)}{\sum_{i=1}^{N_g}\sum_{j=1}^{N_g} K_{r,\gamma}(i,j)}$$

After the calculation GLCM for each element of the image, multiple features can be estimated for each GLCM, such as for example (Soh and Tsatsoulis, 1999):

1.) Energy: $f_1 = \sum_i \sum_j P(i,j)^2$

2.) Contrast: $f_2 = \sum_{n=0}^{Ng-1} n^2 \{\sum_{i=1}^{Ng} \sum_{j=1}^{Ng} P(i,j) || i-j| = n\}$

3.) Correlation: $f_3 = \{\sum_i \sum_j (i,j)P(i,j) - \mu_x \mu_y\} / \{\sigma_x \sigma_y\}$, where μ and σ are the mean and standard deviations for the rows and columns of the matrix.

4.) Homogeneity: $f_4 = \sum_i \sum_j (\frac{1}{1+(i-j)^2})P(i,j)$

5.) Entropy: $f_5 = -\sum_i \sum_j P(i,j)\log(P(i,j))$

6.) Autocorrelation: $f_6 = \sum_i \sum_j (i,j)P(i,j)$

and others. The available, MATLAB image processing toolbox and GLCM Features1 (or 4) codes[1] allows calculation of 22 different GLCM features (Table 3).

The set of these features estimated for each sub-image $[N_y, N_y]$ finally provides the corresponding two-dimensional maps, which can be collocated and correlated with available sea ice observation and after that utilized for the identification different types of floes.

After GLCM analysis, the available in situ dataset can collocated with maps of different GLCM features and analyzed in order to define the GLCM features which can be used for ice floe type identification. The combination of the most successful GLCM features can be further used for the training supervised learning algorithm.

The spatial dimensions $[N_x, N_y]$ of the sub-image inherently define the spatial resolution of the GLCM analysis. Obviously, $[N_x, N_y]$ should be large enough in order to derive the statistically meaningful matrix P_{ij}. In our particular case, we utilized $N_x = N_y$=60. It is necessary to note that GLCM analysis is not a fast computational procedure due to necessity of the massive summations for multiple sub-images. At the same time, GLCM analysis algorithm can be easily parallelized for multi-CPU workstations. Also, due to inherent averaging with order ~ $O(N_x)$, the estimation of the GLCM matrix can be done for every N_x –th pixel of the SAR image. That significantly reduces computational resources needed for the analysis of the SAR images.

4.2 Texture analysis using gradient tensor analysis.

In addition to the "conventional" GLCM-texture analysis, we investigated several additional features to classify SAR images, which are described below. In particular we estimated σ^o values, spatial function of the anisotropy, gradient and coherence directly from the normalized grey-level images. After the incident angle normalization, the estimation of the σ^o is straightforward. The estimation of the anisotropy, squared gradient and coherence can be derived from the eigenvalues of the of the autocovariance matrix of the gradient vector pairs (Vliet and Verbeek, 1995, Bazen and Gerez, 2000):

[1] For example, https://www.mathworks.com/matlabcentral/fileexchange/22354-glcm_features4-m-vectorized-version-of-glcm_features1-m-with-code-changes, recovered April 24 2019.

$$\mathbf{G} = \mathbf{g} \times \mathbf{g}' = \begin{vmatrix} g_x^2 & g_x g_y \\ g_x g_y & g_y^2 \end{vmatrix}, \quad \lambda_{1,2} = 0.5\left(g_x^2 + g_y^2\right) \pm 0.5\left[\left(g_x^2 - g_y^2\right)^2 + 4\left(g_x g_y\right)^2\right]^2,$$

$$Gradient = \lambda_1 + \lambda_2$$

$$Anisotropy = \frac{max(\lambda_1, \lambda_2) - min(\lambda_1, \lambda_2)}{max(\lambda_1, \lambda_2)}$$

$$Coherence = \left[\left(g_x^2 - g_y^2\right)^2 + 4\left(g_x g_y\right)^2\right]^{0.5} / \left(\left(g_x^2 + g_y^2\right)\right.$$

The corresponding spatial maps were derived through the analysis of the autocovariance matrix of the gradient calculated for the each sub-image *[N_y , N_y].*

The list of all features (GLCMs and gradient tensor analyses) utilized in present work is shown in Table 3.

Table 3. The list of all features calculated for SAR images. The features estimated from GLCM and gradient tensor are shown by **bold** and *italic* fonts respectively**.**

1.	**Autocorrelation**	**14**	**Sum average**
2.	**Contrast**	**15**	**Sum variance**
3.	**Correlation(1)**	**16**	**Sum entropy**
4.	**Correlation(2)**	**17**	**Difference variance**
5.	**Cluster Prominence**	**18**	**Difference entropy**
6	**Cluster Shade**	**19**	**Information measure of correlation(1)**
7	**Dissimilarity**	**20**	**Informaiton measure of correlation(2)**
8	**Energy**	**21**	**Inverse difference (INV)**
9	**Entropy**	**22**	**Inverse difference normalized (INN)**
10	**Homogeneity(1):**	23	*Sigma°*
11	**Homogeneity(2):**	24	*Anisotropy*
12	**Maximum probability**	25	*Gradient*
13	**Sum of squares: Variance**	26	*Coherence*

5. Support Vector Machine

"Support Vector Machine" (SVM) is a supervised machine learning algorithm which is mostly used for solving the classification problems (Vapnik , 1982, 1995). The method has been widely applied to different machine vision application and satellite image classifications (Joachims, 1998, Gualtiery and Cromp, 1998) including ice classification (Subashini et al., 2014, Su et al., 2015).

Formally, SVM finds the maximum margin hyperplane that separates the two classes, and can be formulated as a constrained quadratic minimization problem (Vapnik , 1982). The application of the SVM results in two datasets that can be separated by a linear classifier. The process enables the classification of remote sensing datasets which are usually nonlinearly separable in the input space. In case of non-separable data sets, the risk of mis-classification is minimized by maximizing the margin between the two data sets and the separable boundary (Mashao, 2004). It is possible to show that SVM algorithm can be considered as a two-layer neural network.

Advantages of SVM include: (1) SVM solves a quadratic minimization problem, so its solution will be formally unique and available minimization algorithms will be more efficient; (2) SVM automatically defines the number of neurons in the hidden layer, which is equal to the number of support vectors; (3) The definition of the optimal hyperplane which separate two classes results in the more efficient classification. The major disadvantage of SVM is the instability with respect to the noise in the available datasets.

SVM classification is essentially a binary (two-class) classification approach. The most common approach to adopt SVM for multivariate classification problem is to subdivide the space of the N classes into several two-classes problems. If, for example, the image includes open water, small floes and large floes, we may first separate water and after that provide classification for different ice categories. In practice that requires sequential construction of several SVM algorithms. Currently, SVM toolboxes are available in Matlab, Python and other programming languages. Matlab SVM toolbox was used in this study. The schematic of the application outlined above is shown at Figure 6.

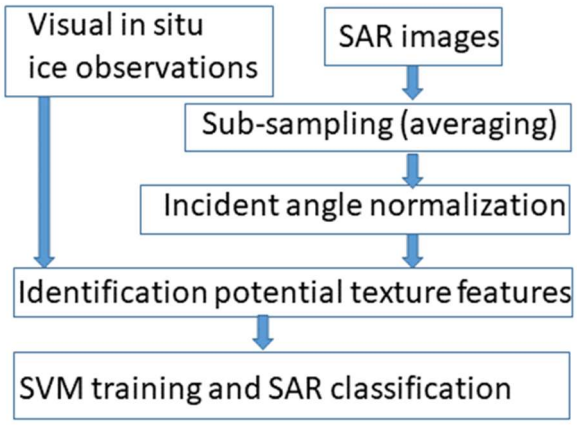

Figure 6. Flow chart of the SAR processing and SAR classification.

6. Results

6.1 Analysis of SAR image texture features at the collocations points

Texture feature analysis depends on the spatial scale of the sea ice surface based on the spatial inhomogeneity of the grey colored image. Formally, SVM may use any number of the texture features, but it is useful to define the most perspective candidates among all available texture features. Ideally perspective texture features should be different for different ice categories and do not correlate between each other.

The available sea ice observations were collocated with available SAR images within ± 1 day temporal window and GLCM analysis was applied to the collocated part of the SAR image with dimension 60x60 pixels. This dimension (30 km) defines the spatial resolution of the GLCM features. Note, that relatively large dimension is consistent with spatial inconsistency between SAR image and collocated ice observation due to time difference and intensive sea ice velocities in the MIZ. Figure 7 show normalized texture values against the different ice floe type. Due to insufficient amount of the vast and large ice floes observations, we combined these sets of the observations together.

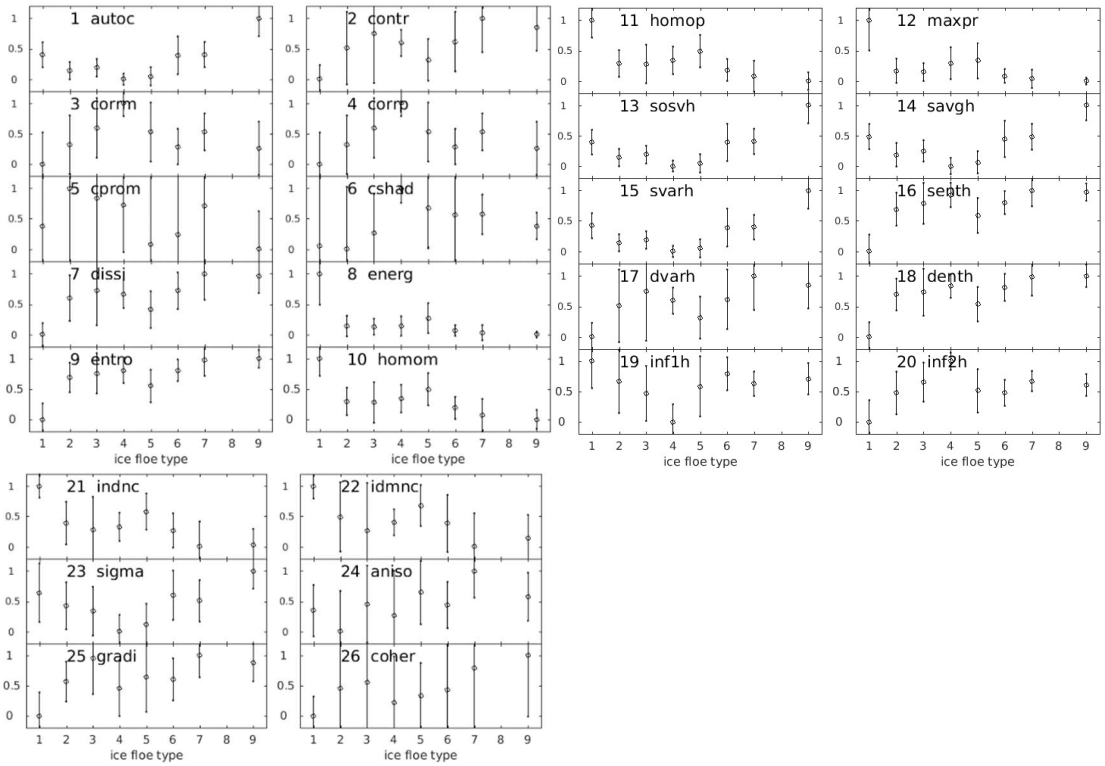

Figure 7. Normalized texture values against the different ice floe type. The corresponding STD are shown. Vast and large sea ice floes observations were combined in in one group. Notation follows numbering given in Table 4, with the following exceptions: 24) aniso=anisotropy, 25) gradi=gradient.

Analysis of the Figure 7 show that multiple texture features can be used for identification of the ice edge. However, the most promising separation between ice and water can be obtained for following texture features: dissipation (7), energy (8), entropy (9), homogeneity (10, 11), maximum probability (12), sum and difference of the entropy (16, 18). But even for these texture features there is some intersection between open water and ice categories.

Another, relatively well-separated category is the combination of the large and vast ice floes category. For this type of the ice, the promising texture features are autocorrelation (1), sum of squares (13), sum of averages (14) and sum of variance (15). Other sea ice floe types cannot be separated from each other using the texture analysis because they have a similar texture values and relatively high STD of the classification, which is based on the available ice floes observations. The large STD is the result of the inconsistency between time of the observation and time of the SAR image which can be within ± 1 day and relatively large sea ice velocity. Besides that, there is extremely high spatial variability of the sea ice floes observations discussed above. Despite this rather disappointing result, the texture features autocorrelation (1) , sum of squares (13), sum of averages (14) and sum of variance (15) have a minimum for the group of the ice types included: pancake ice, new sheet ice, brash/broken ice and cake ice. The typical size of these ice floes categories is less than 20 m. This group of the sea ice floes is the most associated with the MIZ and its identification is important for the proper modeling of the ocean wave attenuation there.

The good identification of the ice edge is obviously due to significant difference in the roughness of the open water surface and ice covered regions. Also, open water regions are well seen on the SAR images and that allows us to provide "open water" observations even without any expert knowledge: the only limitation is the availability of SAR imagery. That allows statistically reliable separation of the open water areas from the ice covered region. The relatively good separation of the large/vast floes is probably due to less intensive variability of the ice field with large/vast floes. That allows one to conduct more accurate collocation between SAR images and sea ice observations.

6.2 Identification of ice floe regions using the SVM

The multiple SVM numerical experiments and visual analysis of the results showed that homogeneity (11) and entropy difference (18) texture features provide the most accurate identification of the open water areas and ice edge. In addition we utilized sea ice passive microwave concentration above 0.4 as the categorical prediction for sea ice classification. The constructed SVM includes linear kernel and uses Sequential Minimal Optimization solver for minimization. The more advanced L1QP solver provided the similar results but require more computational time.

Green lines on Figure 8 shows several examples of the open water-ice classification during the period 10-27 October 2015, and sea ice passive microwave concentration from NOAA/NSIDC. Visual analysis show relatively good overall agreement between SAR based sea ice edge and 0.15 passive microwave sea ice concentration, which is usually treated as an ice edge in the various analyses (Lindsay and Zhang, 2006, Dukhovskoy, et al, 2015). At the same time, in some locations, SAR ice edge differs from microwave 0.15 sea ice concentration by 20-40 km (e.g. 2015/10/15 SAR image at Figure 8b, near 72.4^{o}N, 213^{o}E). Overall, visual analysis of the SAR images suggests that SAR ice edge is more accurate and have a higher resolution.

The next step of our classification is to define the region covered by large-vast floes. The autocorrelation (1) and sum of squares (13) texture features were used for classification. The utilized SVM includes quadratic kernel and uses the L1QP minimization solver. We found that a quadratic solver provides more stable results than conventional Sequential Minimal Optimization algorithm utilized in Matlab. That is probably due to the small volume of the large-vast floes observations available for the SVM training. Several examples of the large-vast floes classification are shown by thick black lines in Figure 8. Note that area of the large-vast floes in the SAR image for 2015/19/27 clearly correspond to the observed large-vast floes.

Finally, the areas covered by category of relatively small (<20 m, pancake-cake) sea ice floes are defined using the SVM with linear kernel and Sequential Minimal Optimization minimization solver. The autocorrelation (1) and average of 14 texture features were used for classification. Previously defined open water and areas covered by large-vast floes were used as a categorical predictor. Several examples of the large-vast floes classification are show in Figure 8: red lines indicate the boundary of this ice type. Note, that area of the relatively small floes at SAR images for 2015/10/10 and 2015/10/15 agrees well with the sea ice observations shown by yellow circles.

The constructed SVMs were applied for all available SAR images for the period of the sea ice observations. Analysis of the agreement between available sea ice observations and SAR images classification revealed that the utilized approach misclassifies about 23% of the relatively small (<20 m, pancake-cake) sea ice floes, 53% of the small-medium sea ice floes observation and 17% of the large-vast sea ice floes observations. 90% of the misclassification of the relatively small (<20m, pancake-cake) sea ice floes are

related to the open water, i.e. these sea ice observations were near the ice edge. All misclassifications of the small-medium floes observations are due to classification of these observations as relatively small (<20 m, pancake-cake) sea ice floes. The misclassifications of the large-vast floes observations are typically due to classification as small-medium sea ice floes. The large volume of small-medium floes misclassifications is probably due to large errors in the texture features values corresponding to the small sea ice floes (Figure 7). Also, as we mentioned above, the spatial distribution of the sea ice floes is very irregular and different sea ice floes were often observed within the distance less than 10-15 km (e.g. SAR 2015/10/27 at Figure 8.). Note also, that 30 km spatial resolution of the calculated GLCMs and relatively small volume of the small/medium floes observations should inevitably result in misclassifications.

Despite the significant levels of misclassifications, the evolution of the sea ice fields at SAR images looks in a reasonable agreement with sea ice velocity fields. Figure 8a, shows that in 10 October 2018, large-vast floes were near 75^{o}N, 200^{o}E. The all sea ice system drifted toward the north-west, but would probably return back to the south according to the sea ice velocities pattern during the 19-27 October 2018. Similarly, the large-vast floes near 74^{o}N, 220^{o}E could drift southward gradually covering the entire region as it seen at Figure 8c,d. This very simple interpretation of the four SAR image pertains to ice advection and does not take into account ice growth/melt and floe welding/fracturing, e.g., the thermodynamic processes which may be responsible for transformation of small sea ice floes into the larger categories.

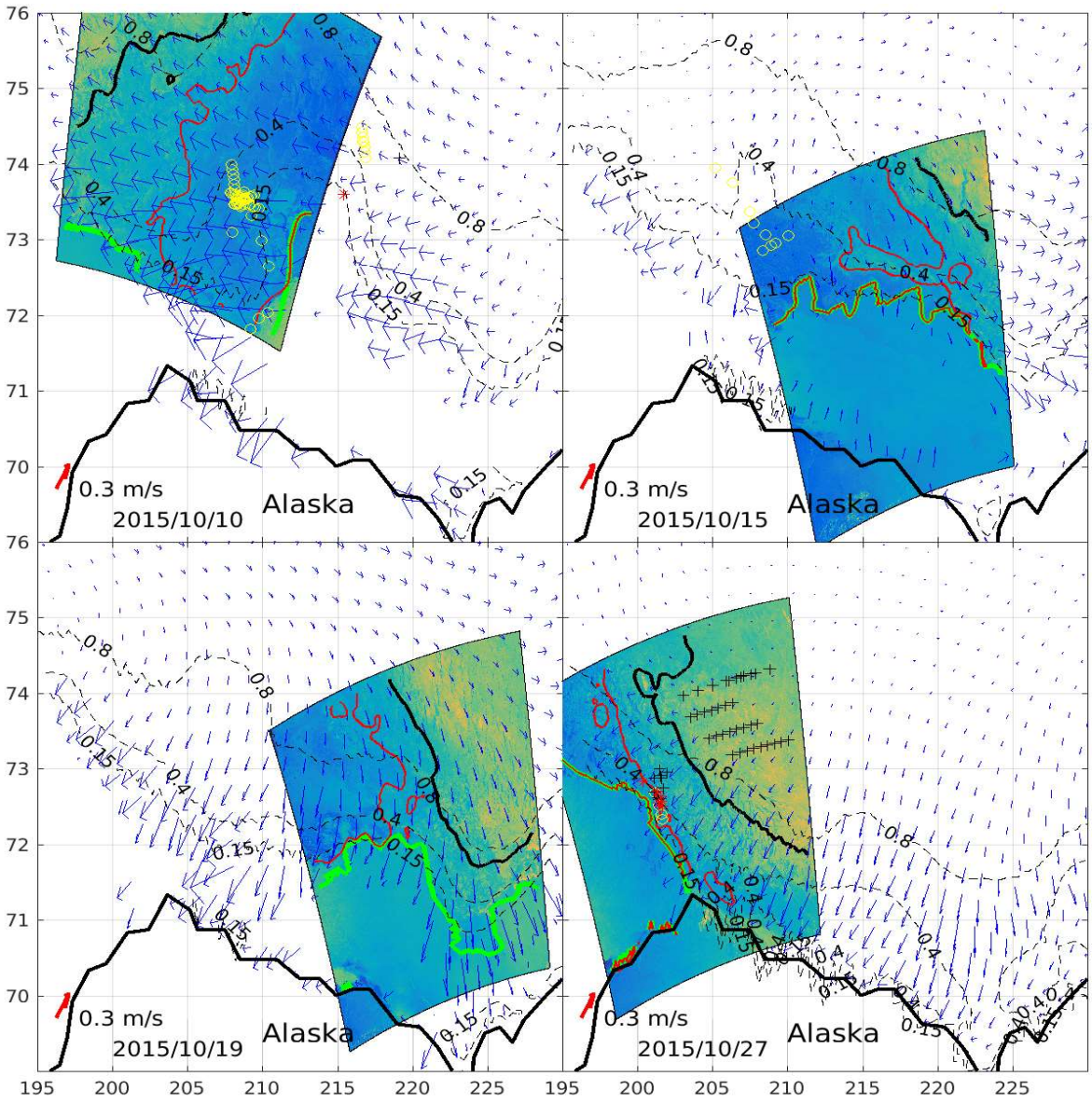

Figure 8. Ice type classification for 20-day period in the Beaufort Sea. Colored lines designate the ice boundaries. Green: boundary between pancake-cake and small-medium ice floes. Red: boundary between small-medium and large-vast ice floes. Yellow circles, red asterisk and black crosses show the observation of the pancake-cake, small-medium and large-vast floes respectively. Blue arrows designate ice velocities from CICE5 model. Dashed lines show the microwave sea ice concentration according to NOAA/NSDIC.

The structure of the GLCM is key component of the applied texture analysis. In order to understand significant level of misclassifications and evaluate future potential of the application of texture analysis for sea ice observations in the MIZ, we calculated mean and corresponding std(GLCM) for each of the sea ice floes categories and open water (Figure 8). Analysis in Figure 8 indicate that open water GLCM have three distinct local peaks, while sea ice categories typically have one or two maximums. This significant GLCM difference explain the rather accurate ice edge classification. Interestingly, the pancake ice GLCM has two local maximums. Location of the first of these maximums coincide with first maximum in open water GLCM. That is probably due to significant presence of the open water in the areas covered by pancake ice and similarity in the backscattering. Note, that new sheet ice GLCM does not have this

maximum and corresponds well to the description of the new sheet ice category, which do not suggest the presence of the open water. Maxima in the broken and cake ice (floes< 20m) GLCMs are only slightly shifted from the first maximum in the open water GLCM suggesting the essential presence of the open water between ice floes.

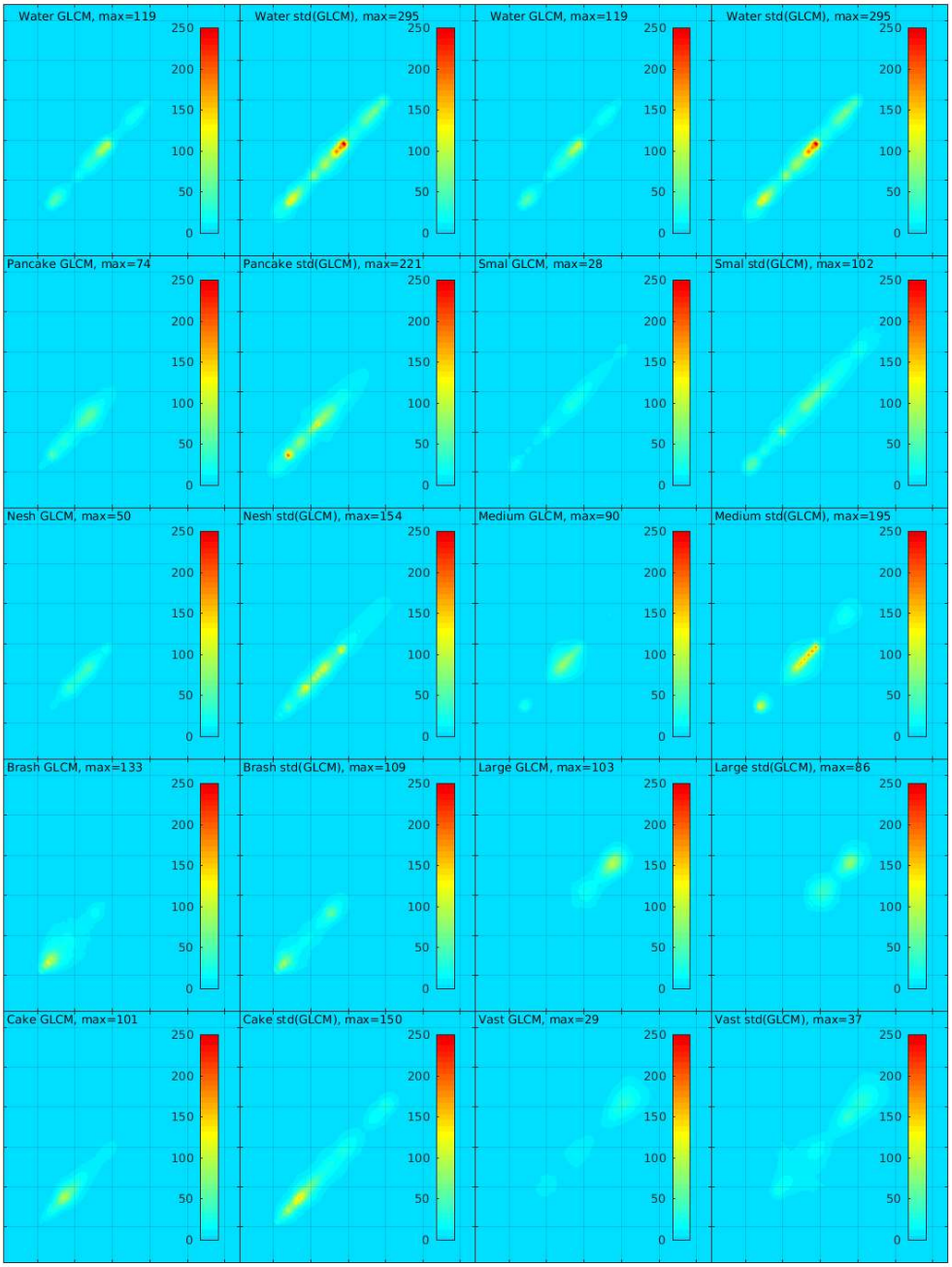

Figure 9. GLCM matrices (64x64) and corresponding STD for open water (top row) and different sea ice floes categories derived from the analysis of the collocated SAR images and sea ice observations.

Location of the maximums in the small and medium floes GLCMs agrees relatively well with the location of the second maximum in the open water GLCM. Similarity of these GLCMs explains similarity of the texture features for these sea ice floe categories. This makes it difficult to separate these ice floes categories in the SAR images. Note also, that medium ice floes GLCMs significantly overlap with pancake

GLCM. That explains why all misclassifications in the identification of the small/medium floes observation are related to the smaller sea ice floes categories.

Large and especially vast sea ice floes GLCMs have a maximums which are significantly shifted from all open water and other sea ice floes categories GLSMs. That explains the relatively good identification of regions covered by large/vast sea ice floes and lower level of misclassification.

The estimated STD of the GLCMs have the similar shape, but typically 1.5-3 times larger than the corresponding GLCMs. Interestingly, open water and pancake have the largest ratio max(STD(GLCM))/ max(GLCM), while for the large and ice floes the similar ratio is minimal. That could be due to intensive dynamical processes (such as ocean waves and ocean currents) which affect backscattering coefficient more intensively in the regions covered by relatively small sea ice floes. Note, that amplitude of the model sea ice velocity in Figure 8 agrees well with this hypothesis. Another impact which probably enlarges STD is variability of the sea ice concentrations, which was not taken into account in our study, due to relatively small volume of the observations.

Besides, these "natural" effects, the most significant errors are probably due to relatively high (20-50 cm/s) sea ice velocities and necessity to use relatively large temporal window (±1 day) for collocating sea ice observations and SAR images. As we mentioned above, that may result in to up to 20-50 km shift and thus contaminate GLCMS by the GLCM from different sea ice categories. Meanwhile, despite all errors and large STDs, Figure 8 shows that there are several groups of the sea ice floes which produce the clearly distinctive GLCM, which can be used for accurate ice floes identifications if we find the way to decrease errors in the GLCM classification.

6.3 Sea ice concentration in the MIZ

Visual sea ice observation from ships (currently in SIGRID-3 format) are the largest available set of the *in situ* (visual) sea ice concentration (IC) observation and formally these data can be used for validation of the available satellite IC products. The scatter plots of the visual IC and IC from three different products with different spatial resolution are shown at Figure 10a,b,d. Coarse resolution IC typically overestimate the visual observation for the IC less than 0.5, while the higher resolution products agree relatively well with visual IC observations for this IC range. Conversely, for IC between 0.5 and 1, coarse resolution IC (Figure 10a) agrees well with visual IC, while higher resolution products typically underestimate IC by 0.1-0.4. The worse agreement was found for MASAM2 IC which underestimates IC by 0.3-0.4 for the visual IC range 0.7-1 (Figure 10b).

The scattered plot for visual IC and IC from CICE5-NCODA DA model run (Figure 10c) suggest that CICE5-NCODA significantly overestimate the IC for the IC range 0.1-0.5. CICE5-NCODA assimilates two kinds (SSMI and AMSR2) of the preprocessed IC shown at Figure 10e, respectively. Interestingly, that for the IC range between 0.1 and 0.5, IC from these products are significantly smaller than CICE5-NCODA output. This suggests that CICE5 model has a significant bias and generates an excessive volume of the ice that result for higher IC and ice thickness. That agrees with the similar conclusion made by Allard at al. 2018 and Yaremchuk at al., 2018. Rogers et al. 2018 also remark on the overprediction of ice by the CICE5 model, specifically for the ONR Sea State case, though the overprediction is not universal: regions of locally underpredicted ice are also noted. The reasons for significant bias in CICE5 model solution are not clear and may be related to the bias in coarse resolution atmospheric forcing which would suggest a necessity for development and application an advanced DA algorithm that would be able to correct CICE5 model

solution. However, if the origin of the errors are in the assimilated fields themselves, this would not help. In fact, this is the conclusion in Rogers et al. (2018) for the October 11-14 case: the CICE5 model is assimilating fields which have not been updated during a period of rapid observed ice retreat, so the retreat is erroneously prevented in the model analyses.

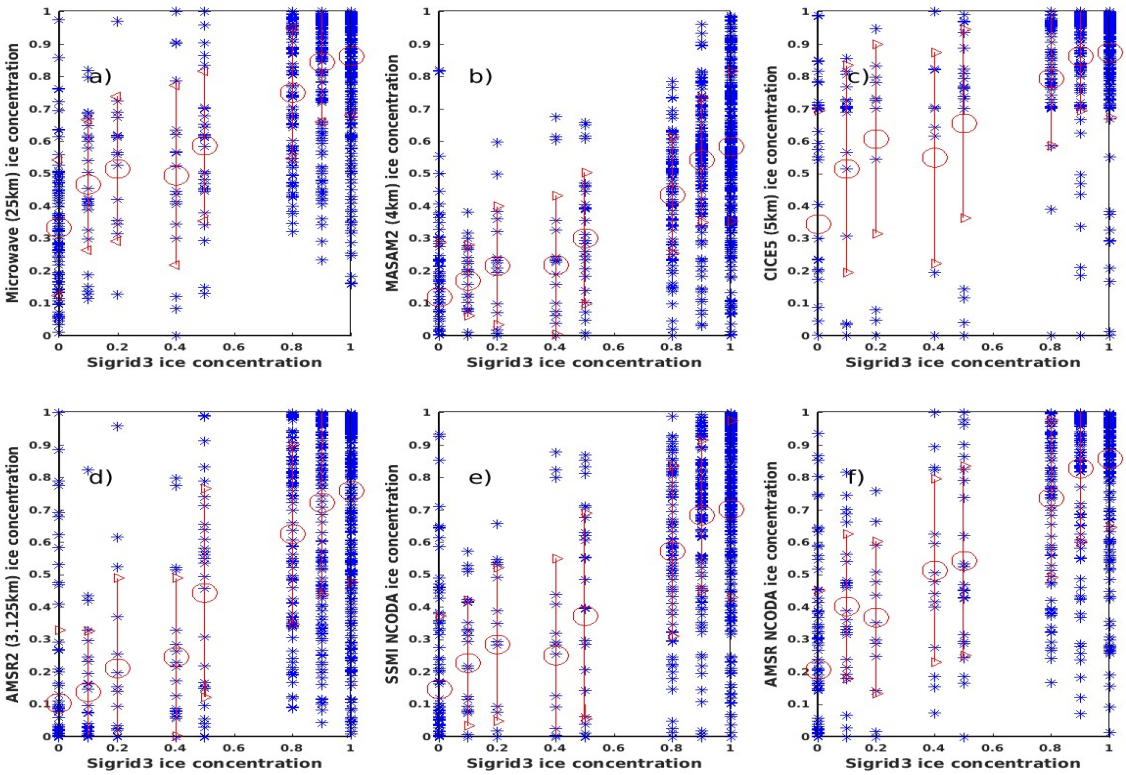

Figure 10. Scattered plot of the visual sea ice observations against: (a) microwave sea ice concentration with 25km resolution;(b) MASAM2 sea ice concentration with 4km resolution; (c) results of the CICE5-NCODA DA model run 5km resolution (c); (d) AMSR-2 sea ice concentration (3.km resolution); (e-f) SSMI and AMSR-2 sea ice concentration utilized for CICE5-NCODA DA respectively. Mean values and STD bars are shown by red circles and triangles respectively.

7. Summary and Conclusions

An approach for automatic detection of the type of the sea ice floes in the MIZ from RADARSAT-2 SAR images with resolution of 50 m has been developed and tested. The approach is based on analysis of the texture features using the GLCM and several additional functions based on the estimates of the averaged gradient tensor and SVM classification algorithm. The major source of the sea ice observation were obtained during the ONR-supported 'Sea State and Boundary Layer Physics' cruise conducted in the Beaufort Sea during September-October 2015 (Thomson et al. 2018). The RADARSAT-2 SAR were specifically acquired through the NIC and UW/APL in order to maximize the size of the collocated points between visual sea ice observations and SAR images.

The preprocessing of the RADARSAT-2 SAR images includes the spatial averaging with spatial window of ten pixels and linear incident angle normalization procedure (Zakhavtkina et al, 2012). The basic goal of our study was to find a way for accurate identification of the sea ice edge and ice type in the MIZ. Because

of that, the backscattering normalization procedure was accomplished for a reference angle of 35^{o} using the linear approximation of the backwatering angular dependence for open water. The type of the ice floes selected for classification included eight types (including open water type and large and vast floes as a one group) according to the SIGRID 3 format (JCOM-TR-023, 2014).

The set of the observations used for SVM training includes the visual observation from ship bridges and "artificial" sea ice floes observations, which were defined after analysis of the real observation and collocated SAR images. The artificial observations were selected in the reasonable spatial and temporal proximity to the real observations in the regions with similar texture properties in the collocated SAR image. The artificial set of the sea ice floes observations was needed because of insufficient volume of the collocated pairs needed for training SVMs.

Twenty two GLCMs and four gradient tensor texture features were calculated for every observation collocated with SAR image in space and ±1 day temporal window. The analysis of texture features and sea ice floe types showed that only open water and large/vast floes are relatively well separated from other floe types for multiple texture features. It was also found that the categories of pancake, new sheet ice, brash/broken ice and cake ice have a reasonable separation from categories of small and medium floes using several texture features. Based on this analysis, the first step of the classification algorithm included sequential identification of the open water, large/vast floes using the conventional SVM. In case of ice edge identification, we also included condition of sea ice concentration larger than 0.4 as an indicator for the presence of the sea ice. After that, the group of the pancake and cake ice was identified using additional SVM. The remaining part of the SAR image was treated as area covered by small and medium floes, whose texture features are similar and cannot be separated.

SAR images taken during October 2015 were used for the sea ice floe identification. The visual analysis revealed that the utilized approach allows accurate identification of the open water which is more accurate than retrieved from the sea ice concentration maps derived from different satellites. In some regions by the location of the ice edge identified from SAR images may differ by 20-50 km from the conventional ice edge identified as 0.15 sea ice concentration.

Statistical analysis showed that that error in large/vast floes observation misclassification do not exceed 17%. The rate of the misclassification for the group of the observations of the pancake-sheet-broken-cake ice was about 26%, with a major portion (70%) of the misclassification related to the open water category. The highest (53%) rate of the misclassification was with the small-medium ice floe observations with the most of the misclassification related to the pancake-sheet-broken-cake categories. Despite a significant rate of misclassification of pancake-sheet-broken-cake ice floes and especially small-medium floes, the visual analysis of the temporal evolution of areas covered by different ice floe groups agrees well with the sea ice velocities from CICE5 model configured for the Beaufort Sea region (Figure 8).

The major source of the inaccuracies in the utilized approach comes from the errors in the spatial and temporal colocation between visual sea ice observations and SAR images. Due to relatively small number of the collocated pairs we had to increase the temporal collocation window up to ±1 day. That, due to 30-60 cm/s velocities in the marginal ice zone may result in differences up to 60 km in the spatial location of the visual sea ice observation and SAR image.

Visual observations of the IC provide the opportunity for the analysis of the available satellite IC product utilized for assimilation. We found that 3.1 km resolution AMSR-2 IC concentration provide fair estimates of the IC in the MIZ with small bias for the 0.6-1.0 IC range (Figure 10d,f). SSMI IC observations are less

accurate. The worse agreement was obtained for the MASAM2 IC observations (Figure 10b). The results of the CICE5-NCODA DA model run (Figure 10c) shows that despite the assimilation of the AMSR2 and SSMI IC observation, CICE5-NCODA DA system generate excessive sea ice volume. Overestimation of ice in the MIZ will inevitable affect the attenuation of the ocean waves and because of that, this problem should be addressed using alternative products in order to achieve more accurate ocean wave hindcast in the MIZ.

Acknowledgments

Authors GP and WER were supported by the Office of Naval Research via the NRL Core program, Program Element Number 62435N, the 6.2 project 'Wave-ice interactions'.

This is NRL contribution NRL/MR/7320-19-9903 and is approved for public release.

References:

Allard, R. A., Sinead L.Farrell, S.L., Hebert[a], D. A.,Johnston, W. F., Li, L., Kurtz, N.T., Phelps, M.W., Pamela G. Posey Phelps, M.W., Pamela G.Posey, P.G.,Tilling, R., Ridout, A., Wallcraft, A.J. (2018). Utilizing CryoSat2 sea ice thickness to initialize a coupled ice-ocean modeling system. *Adv. Space. Res*., (62), Issue 6, 1265-1280.

Ardhuin, F., P. Sutherland, M. Doble, and P. Wadhams, Ocean waves across the Arctic (2016): Attenuation due to dissipation dominates over scattering for periods longer than 19 s, Geopys. Res. Lett., 43, 5775–5783, doi:10.1002/2016GL068204.

Askne, J., A. Carlstrom, W. Dierking, and L. Ulander, (1994). ERS-1 SAR backscatter modeling and interpretation of sea ice signatures, in Proc. IGARSS, Pasadena, CA, Aug. 8–12, 1994, pp. 162–164.

Bazen Asker M. and Sabih H. Gerez (2000) Directional Field Computation for Fingerprints Based on the Principal Component Analysis of Local Gradients, ProRISC 2000 Workshop on Circuits, Systems and Signal Processing, Veldhoven, The Netherlands, November.

Bogdanov Andrey V., Stein Sandven, Ola M. Johannessen, Vitaly Yu. Alexandrov, and Leonid P. Bobylev, (2005) Multisensor Approach to Automated Classification of Sea Ice Image Data*in* IEEE Transactions on Geoscience and Remote Sensing 43(7):1648-1664, DOI: 10.1109/TGRS.2005.846882.

Cheng, S., W.E. Rogers, J. Thomson, M. Smith, M.J. Doble, P. Wadhams, A.L. Kohout, B. Lund, O.P.G. Persson, C.O. Collins III, S.F. Ackley, F. Montiel, and H.H. Shen, 2017: Calibrating a Viscoelastic Sea Ice Model for Wave Propagation in the Arctic Fall Marginal Ice Zone. J. Geophys. Res. Oceans, 122, doi://10.1002/2017JC013275.

Clausi, D., (2002) An analysis of co-occurrence texture statisticsas a function of grey level quantization, *Can. J.* Remote Sensing, Vol. 28, No. 1, pp. 45–62.

Cummings, J., O. Smedstad. (2013). Variational data assimilation for the global ocean. In: *Data Assimilation for Atmospheric, Oceanic and Hydrological Applications*, (Park, S.K. & L. Xu, Eds.), Vol. 2, pp. 303–343, Springer, Berlin, doi:10.1007/978--3-642-35088-7_13.

Doble M., P.Wadhams, (2006) Dynamical contrasts between pancake and pack ice, investigated with a drifting buoy array, J.Geoph. Res.(111), C11S24, doi:10.1029/20.

Doble, M. J. (2009) Simulating pancake and frazil ice growth in the Weddell Sea: A process model from freezing to consolidation, J. Geophys. Res., 114, C09003, doi:10.1029/2008JC0.

Doble M.J., G. De Carolis, M.H. Meylan, J-R Bidlot, and P. Wadhams, (2015) Relating wave attenuation to pancake ice thickness, using field measurements and model results, Geoph. Res. Let, 42, 4473–4481, doi:10.1002/2015GL063628.

Dierking, W, (2010) "Mapping of different sea ice regimes using images from Sentinel-1 and ALOS synthetic aperture radar," *IEEE Trans. Geosci. Remote Sens.*, vol. 48, no. 3, pp. 1045–1058, Mar. 2010.

De Abreu, R. (2000) "RADAR sea ice signatures: An operational primer," in *Proc. Workshop Mapping Archiving Sea Ice Data—The Expanding Role Radar*, Ottawa, ON, Canada, May 2–4, 2000, pp. 85–94,JCOMM Tech. Rep. no. 7.

Dukhovskoy, D. S., J. Ubnoske,E. Blanchard-Wrigglesworth,H. R. Hiester, and A. Proshutinsky, (2015). Skill metrics for evaluation and comparison of sea ice models, J. Geophys. Res. Oceans,120, 5910–5931, doi:10.1002/2015JC010989.

Gualtieri, J. A., and Cromp, R. F. 1998. Support vector machines for hyperspectral remote sensing classification. In Proceedings of the 27th AIPR Workshop: Advances in Computer Assisted Recognition, Washington, DC, Oct.14th -16th October, 1998 (Washington, DC: SPIE), pp. 221–232.

Haralick, R. M., K. Shanmugan, and I. H. Dinstein, (1973), "Textural features for image classification," *IEEE Trans. Syst., Man, Cybern.,* vol. SMC-3, pp. 610–621, May 1973.

Hunke, E.C., Lipscomb, W.H. (2008). CICE: The Los Alamos Sea Ice Model, Documentation and Software User's Manual, Version 4.0. Tech. Rep. LA-CC-06-012, Los Alamos National Laboratory, Los Alamos, New Mexico. Available from: <http://climate.lanl.gov/Models/CICE>.

Hogan, T.F., M. Liu, J.A. Ridout, M.S. Peng, T.R. Whitcomb, B.C. Ruston, C.A. Reynolds, S.D. Eckermann, J.R. Moskaitis, N.L. Baker, J.P. McCormack, K.C. Viner, J.G. McLay, M.K. Flatau, L. Xu, C. Chen, & S.W. Chang. (2014). The Navy Global Environmental Model. *Oceanography 27*(3):116–125, http://dx.doi.org/10.5670/oceanog.2014.73.

Joachims, T. (1998). Text categorization with support vector machines—learning with many relevant features. In Proceedings of the 10th European Conference on Machine Learning, Chemnitz, Germany. (Berlin: Springer), pp. 137–142.

JCOMM-TR-023, (2014) WMO/TD-NO.1214, SPA_ETSI_general_SIM01 SIGRID-3: A Vector Archive Format For Sea Ice Georeferenced Information And Data, https://www.jcomm.info/index.php?option=com_oe&task=viewDocumentRecord&docID=4439.

Komarov, A. and D. G. Barber, (2014) Sea Ice Motion Tracking From Sequential Dual-Polarization RADARSAT-2 Images, IEEE TRANSACTIONS ON GEOSCIENCE AND REMOTE SENSING, VOL. 52,(121(), NO. 1, JANUARY 2014

Kwok R. and G. F. Cunningham, (2004) "Backscatter characteristics of the winter ice cover in the Beaufort Sea," *J. Geophys. Res.*, vol. 99, no. C4, pp. 7787–7802, Apr. 1994.

Mashao D. (2004). Comparing SVM and GMM on parametric feature-sets. In Proceedings of the 15th Annual Symposium of the Pattern Recognition Association of South Africa, Cape Town, South Africa. 27th – 29th November 2004.

Lee Jong-Sen, Eric Pottier, (2009) Polarimetric Radar Imaging: From Basics to Applications CRC Press 438 Pages - 197 B/W Illustrations ISBN 9781420054972 - CAT# 5497X.

Murashkin D., G. Spreen, M. Huntemann, W. Dierking, (2018). Method for detection of leads from Sentinel-1 SAR images Annals of Glaciology / Volume 59 (76) https://doi.org/10.1017/aog.2018.6.

Squire VA, Montiel F. (2016). Evolution of directional wave spectra in the marginal ice zone:a new model tested with legacy data. *J. Phys. Oceanogr.* **46**, 3121–3137. (doi:10.1175/JPOD-16-0118.1).

Squire VA. (2018). A fresh look at how ocean waves and sea ice interact.Phil. Trans. R. Soc. A 376: 20170342. http://dx.doi.org/10.1098/rsta.2017.0342, 2018

Soh, Leen-Kiat and Tsatsoulis, Costas, (1999). "Texture Analysis of SAR Sea Ice Imagery Using Gray Level Co-Occurrence Matrices" . *CSE Journal Articles*. 47. http://digitalcommons.unl.edu/csearticles/47.

Su Hua, Yunpeng Wang, Jie Xiao, Xiao-Hai Yan, (2015). Classification of MODIS images combining surface temperature and texture features using the Support Vector Machine method for estimation of the extent of sea ice in the frozen Bohai Bay, China in International Journal of Remote Sensing, 36(10): 2734-2750, DOI: 10.1080/01431161.2015.1041619.

Subashini P., Krishnaveni M., Ane B.K., Roller D. (2014). SVM-Based Classification for Identification of Ice Types in SAR Images Using Color Perception Phenomena. In: Abraham A., Krömer P., Snášel V. (eds) Innovations in Bio-inspired Computing and Applications. Advances in Intelligent Systems and Computing, vol 237. Springer, Cham.

Topouzelis Konstantinos , Suman Singha, and Dimitra Kitsiou (2016). Incidence angle Normalization of Wide Swath SAR Data for Oceanographic Applications, Open Geosci. ; 8:450–464.

Van Vliet, Lucas J., and Piet W. Verbeek (1995). ASCI'95, Proceedings of the first Conference of the Advanced School for Computing and Imaging, Heijen (The Netherlands), May 16-18, 1995, pp. 442-450.

Vapnik, V.N. (1982). Estimation of Dependences Based on Empirical Data, Addendum 1, New York: SpringerVerlag.

Vapnik, V. N. (1995). *The Nature of Statistical Learning Theory*, Springer-Verlag, ISBN 0-387-98780-0, 1995.

Wang R, Shen HH, (2010). Gravity waves propogation into an ice-covered ocean: a model. *J. Geophs. Res.*, 115, C06024, (doi:10.1029/2009jc005591).

Williams, T. D., Bennetts, L. G., Squire, V. A., Dumont, D., and Bertino, L. (2013a): Wave-ice interactions in the marginal ice zone. Part 1: Theoretical foundations, Ocean Model., 71, 81–91, https://doi.org/10.1016/j.ocemod.2013.05.010.

Williams, T. D., Bennetts, L. G., Squire, V. A., Dumont, D., and Bertino, L. (2013b): Wave-ice interactions in the marginal ice zone. Part 2: Numerical implementation and sensitivity studies along 1D transects of the ocean surface, Ocean Model., 71, 92–101, https://doi.org/10.1016/j.ocemod.2013.05.011.

Williams, T.D. P. Rampal, and S. Bouillon. (2017). Wave–ice interactions in the neXtSIM sea-ice model, The Cryosphere, 11, 2117–2135, https://doi.org/10.5194/tc-11-2117-2017.

Yaremchuk M., T. Townsend, G. Panteleev, D. Hebert, and R. Allard: (2018). Advances in the short-term Forecasting of ice conditions in the Beaufort Sea,. *J. Geophys. Research, (submitted 09/18/2018)*

Zakhvatkina N. Yu., Vitaly Yu. Alexandrov, Ola M. Johannessen, Stein Sandven, and Ivan Ye. Frolov, (2013). Classification of Sea Ice Types in ENVISATSynthetic Aperture Radar Images, *in* IEEE Transactions on Geoscience and Remote Sensing 51(5), 2587-2600.

Zakhvatkina N., Anton Korosov, Stefan Muckenhuber, Stein Sandven, Mohamed Babiker, (2016). Operational algorithm for ice/water classification on dual-polarized RADARSAT-2 images, The Cryosphere Discuss., doi:10.5194/tc-2016-131.

Zhang, J., R.W. Lindsay, (2006). Assimilation of Ice Concentration in an Ice–Ocean Model, JAOT, 742-749.